J|A|C|S
ARTICLES
Published on Web 08/11/2007

Catalytic Efficiency of Iron(III) Oxides in Decomposition of Hydrogen Peroxide: Competition between the Surface Area and Crystallinity of Nanoparticles

Martin Hermanek, Radek Zboril,* Ivo Medrik, Jiri Pechousek, and Cenek Gregor

Contribution from the Centre for Nanomaterial Research, Palacky University, Slechtitelu 11, 783 71 Olomouc, and Departments of Experimental Physics and Physical Chemistry, Palacky University, Svobody 26, 771 46 Olomouc, Czech Republic

Received April 26, 2007; E-mail: zboril@prfnw.upol.cz

Abstract: Various iron(III) oxide catalysts were prepared by controlled decomposition of a narrow layer (ca. 1 mm) of iron(II) oxalate dihydrate, $FeC_2O_4 \cdot 2H_2O$, in air at the minimum conversion temperature of 175 °C. This thermally induced solid-state process allows for simple synthesis of amorphous Fe_2O_3 nanoparticles and their controlled one-step crystallization to hematite (α-Fe_2O_3). Thus, nanopowders differing in surface area and particle crystallinity can be produced depending on the reaction time. The phase composition of iron(III) oxides was monitored by XRD and ^{57}Fe Mössbauer spectroscopy including in-field measurements, providing information on the relative contents of amorphous and crystalline phases. The gradual changes in particle size and surface area accompanying crystallization were evaluated by HRTEM and BET analysis, respectively. The catalytic efficiency of the synthesized nanoparticles was tested by tracking the decomposition of hydrogen peroxide. The obtained kinetic data gave an unconventional nonmonotone dependence of the rate constant on the surface area of the samples. The amorphous nanopowder with the largest surface area of 401 $m^2\ g^{-1}$ revealed the lowest catalytic efficiency, while the highest efficiency was achieved with the sample having a significantly lower surface area, 337 $m^2\ g^{-1}$, exhibiting a prevailing content of crystalline α-Fe_2O_3 phase. The obtained rate constant, $26.4 \times 10^{-3}\ min^{-1}\ (g/L)^{-1}$, is currently the highest value published. The observed rare catalytic phenomenon, where the particle crystallinity prevails over the surface area effects, is discussed with respect to other processes of heterogeneous catalysis.

1. Introduction

The immense popularity of iron oxides as catalysts originates from their broad application potential due to easy handling, relatively low cost, nontoxicity, and environmentally friendly character. Iron oxide catalysts are currently utilized on a large scale in laboratory, industrial, and environmental processes. They are used to accelerate various reactions including oxidation of carbon monoxide,[1−3] decomposition of soot and NO_x in diesel exhausts,[4−6] reduction of nitrogen oxides[7] and sulfur dioxide[8] by CO, photocatalytic splitting of water,[9] Fischer−Tropsch synthesis of hydrocarbons,[10] catalytic decomposition of industrial dyes,[11,12] water−gas shift reactions,[13,14] nucleation of diamonds,[15] conversions of phenolic and other environmentally harmful aromatic compounds,[16−18] dehydrogenation of ethylbenzene to styrene,[19−24] and catalytic oxidations of other various organic compounds.[25−32]

Catalytic decomposition of H_2O_2 is extensively studied due to its vast applicability in water treatment technologies; various organic waters and soil pollutants can be successfully oxidized and degraded by hydrogen peroxide promoted by iron oxides.[33−54]

The kinetics of hydrogen peroxide decomposition depends mainly on experimental conditions such as pH, concentrations of hydrogen peroxide, and the catalyst. In the case of hetero-

(1) Li, P.; Miser, D. E.; Rabiei, S.; Yadav, R. T.; Hajaligol, M. R. *Appl. Catal., B* **2003**, *43*, 151−162.
(2) Dondur, V.; Radic, N.; Grbic, B.; Drofenik, M. *Mater. Sci. Forum* **2006**, *518*, 85−90.
(3) Khedr, M. H.; Halim, K.; Nasr, M. I.; El-Mansy, A. M. *Mater. Sci. Eng., A* **2006**, *430*, 40−45.
(4) Kureti, S.; Hizbullah, K.; Weisweiler, W. *Chem. Eng. Technol.* **2003**, *26*, 1003−1006.
(5) Kureti, S.; Weisweiler, W.; Hizbullah, K. *Appl. Catal., B* **2003**, *43*, 281−291.
(6) Balle, P.; Bockhorn, H.; Geiger, B.; Jan, N.; Kureti, S.; Reichert, D.; Schroder, T. *Chem. Eng. Process.* **2006**, *45*, 1065−1073.
(7) Randall, H.; Doepper, R.; Renken, A. *Appl. Catal., B* **1998**, *17*, 357−369.
(8) Wang, X. H.; Wang, A. Q.; Li, N.; Wang, X. D.; Liu, Z.; Zhang, T. *Ind. Eng. Chem. Res.* **2006**, *45*, 4582−4588.
(9) Gondal, M. A.; Hameed, A.; Yamani, Z. H.; Suwaiyan, A. *Appl. Catal., A* **2004**, *268*, 159−167.
(10) Kim, D. J.; Dunn, B. C.; Huggins, F.; Huffman, G. P.; Kang, M.; Yie, J. E.; Eyring, E. M. *Energy Fuels* **2006**, *20*, 2608−2611.
(11) Herrera, F.; Lopez, A.; Mascolo, G.; Albers, E.; Kiwi, J. *Appl. Catal., B* **2001**, *29*, 147−162.
(12) Herrera, F.; Lopez, A.; Mascolo, G.; Albers, P.; Kiwi, J. *Water Res.* **2001**, *35*, 750−760.
(13) Basinska, A.; Maniecki, T. P.; Jozwiak, W. K. *React. Kinet. Catal. Lett.* **2006**, *89*, 319−324.
(14) Silberova, B. A. A.; Mul, G.; Makkee, M.; Moulijn, J. A. *J. Catal.* **2006**, *243*, 171−182.
(15) Qin, J. M.; Ma, H. A.; Chen, L. X.; Tian, Y.; Zang, C. Y.; Ren, G. Z.; Guan, Q. F.; Jia, X. *Diamond Relat. Mater.* **2006**, *15*, 1369−1373.
(16) Shin, E. J.; Miser, D. E.; Chan, W. G.; Hajaligol, M. R. *Appl. Catal., B* **2005**, *61*, 79−89.
(17) Lauwiner, M.; Rys, P.; Wissmann, J. *Appl. Catal., A* **1998**, *172*, 141−148.
(18) Lauwiner, M.; Roth, R.; Rys, P. *Appl. Catal., A* **1999**, *177*, 9−14.

geneous catalysis, moreover, the structure and surface properties of catalysts have to be taken into account.

It is generally accepted that lower pH values (2−4) are favorable for classical Fenton-like reactions performed with soluble Fe(II) homogeneous catalysts,[53] yet two disadvantages accompanying the reactions are the acidic environment itself and the necessary separation of the dissolved iron from the reactive solution after process completion. The two limitations can be avoided if heterogeneous catalysts such as pure metals (e.g., Ag, Cu, Fe, Mn, Ni, and Pt) or their oxides (including various iron(III) oxides) are used.[42] These heterogeneous catalysts can be effectively used at neutral pH and can be easily separated by physical sedimentation after reaction completion. The acidic environment however should be avoided because leaching of iron oxides can cause a loss in catalytic activity.[34] Higher pH values on the other hand cause higher decomposition rates.[40,44] The role of the iron(III) oxide catalyst concentration (number of surface reaction sites) on the rate of the hydrogen peroxide decomposition is very clear: the decomposition rate is directly proportional to the iron oxide concentration.[44] Moreover, higher rates of H_2O_2 decomposition are directly related to higher decomposition rates of the target pollutants.[39]

Generally, the principal factor determining catalytic efficiency in heterogeneous catalysis is the sufficiently large surface area, which can be achieved by the use of either nanoparticles or granular particles with porous character. Thus, the highest rate constants so far achieved were reported for poorly ordered ferrihydrite and porous goethite (α-FeOOH);[37,42,52] however, objective comparison of any kinetic data is rather complicated due to the different pH conditions at which the data were obtained. Unfortunately, the literature data discuss only marginally the catalytic efficiency from the viewpoint of the structure and crystallinity of the catalyst particles, although various iron oxides (hematite, goethite, ferrihydrite, maghemite, lepidocrocite, akaganéite, magnetite) differing in these characteristics were tested. A comparative study of the catalytic efficiency in the decomposition reaction of hydrogen peroxide using different iron(III) oxides was performed by Huang et al.[42] The highest activity was achieved with amorphous ferrihydrite possessing the largest surface area followed by crystalline oxides—needlelike goethite and platelike hematite with the lowest surface area. The rate constant observed for ferrihydrite was 2 orders of magnitude higher than for the other two iron oxides. However, when normalized with surface area, the differences in the measured rate constants became far less significant.

Similar results were obtained by Valentine and Wang,[52] who again achieved the highest catalytic activity with amorphous ferrihydrite possessing the largest surface area among the studied iron(III) oxide catalysts.

The fundamental problem in examination of whether amorphous or crystalline materials are more efficient in the catalysis processes is that all works dealing with this topic compare materials of different natures, prepared by various experimental routes, and carrying different histories depending on the used precursors. Hence, to gain better insight into the role of the catalyst crystallinity, we monitored the degree of crystallinity of the iron(III) oxide (hematite), prepared by thermally induced decomposition of ferrous oxalate dehydrate, for different periods of time in the hydrogen peroxide decomposition under constant reaction conditions (pH, concentrations of iron oxide and H_2O_2).

As a result, we report the unique behavior of iron(III) oxide nanoparticles, the catalytic efficiency of which is strongly determined by the crystallinity of the particles rather than by their surface area. This phenomenon of the local increase in the catalytic activity with particle crystallinity and the general effect of the "surface quality", prevailing over the commonly accepted key role of a large surface area, are discussed with respect to other processes of heterogeneous catalysis. A similar principal effect of the crystal structure of the iron oxide catalysts on the kinetics of the hydrogen peroxide decomposition will be reported soon.

2. Materials and Methods

2.1. Synthesis of the Catalysts. Iron(II) oxalate dihydrate, $FeC_2O_4 \cdot 2H_2O$ (Sigma-Aldrich) was used as a suitable precursor for the solid-state syntheses of iron(III) oxide-based nanocatalysts differing in the surface area and crystallinity of the particles. Before the thermal treatment, the precursor was finely homogenized in an agate mortar. Next 1 g of the powdered precursor was spread on the bottom of a crucible in a thin layer (ca. 1 mm thick) and heated in air at the

(19) Badstube, T.; Papp, H.; Kustrowski, P.; Dziembaj, R. *Catal. Lett.* **1998**, *55*, 169−172.
(20) Badstube, T.; Papp, H.; Dziembaj, R.; Kustrowski, P. *Appl. Catal., A* **2000**, *204*, 153−165.
(21) Huang, W. X.; Ranke, W.; Schlogl, R. *J. Phys. Chem. B* **2005**, *109*, 9202−9204.
(22) Shekhah, O.; Ranke, W.; Schule, A.; Kolios, G.; Schlogl, R. *Angew. Chem., Int. Ed.* **2003**, *42*, 5760−5763.
(23) Weiss, W.; Schlogl, R. *Top. Catal.* **2000**, *13*, 75−90.
(24) Wong, S. T.; Lee, J. F.; Cheng, S. F.; Mou, C. Y. *Appl. Catal., A* **2000**, *198*, 115−126.
(25) Murai, K. I.; Tomita, K.; Tojo, S.; Moriga, T.; Nakabayashi, I. *Int. J. Mod. Phys. B* **2006**, *20*, 4249−4254.
(26) Tanaka, S.; Nakagawa, K.; Kanezaki, E.; Katoh, M.; Murai, K.; Moriga, T.; Nakabayashi, I.; Sugiyama, S.; Kidoguchi, Y.; Miwa, K. *J. Jpn. Pet. Inst.* **2005**, *48*, 223−228.
(27) Arena, F.; Gatti, G.; Stievano, L.; Martra, G.; Coluccia, S.; Frusteri, F.; Spadaro, L.; Parmaliana, A. *Catal. Today* **2006**, *117*, 75−79.
(28) Kovalenko, V. V.; Rumyantseva, M. N.; Gaskov, A. M.; Makshina, E. V.; Yushchenko, V. V.; Ivanova, I. I.; Ponzoni, A.; Faglia, G.; Comini, E. *Inorg. Mater.* **2006**, *42*, 1088−1093.
(29) Van Devener, B.; Anderson, S. L. *Energy Fuels* **2006**, *20*, 1886−1894.
(30) Perkas, N.; Koltypin, Y.; Palchik, O.; Gedanken, A.; Chandrasekaran, S. *Appl. Catal., A* **2001**, *209*, 125−130.
(31) Perkas, N.; Wang, Y. Q.; Koltypin, Y.; Gedanken, A.; Chandrasekaran, S. *Chem. Commun.* **2001**, *11*, 988−989.
(32) Perkas, N.; Palchik, O.; Brukental, I.; Nowik, I.; Gofer, Y.; Koltypin, Y.; Gedanken, A. *J. Phys. Chem. B* **2003**, *107*, 8772−8778.
(33) Al-Hayek, N.; Dore, M. *Water Res.* **1990**, *24*, 973−982.
(34) Dantas, T.; Mendonca, V. P.; Jose, H. J.; Rodrigues, A. E.; Moreira, R. *Chem. Eng. J.* **2006**, *118*, 77−82.
(35) Khan, A. J.; Watts, R. J. *Water, Air, Soil Pollut.* **1996**, *88*, 247−260.
(36) Lin, S. S.; Gurol, M. D. *Water Sci. Technol.* **1996**, *34*, 57−64.
(37) Lin, S. S.; Gurol, M. D. *Environ. Sci. Technol.* **1998**, *32*, 1417−1423.
(38) Wang, D. A.; Liu, Z. Q.; Liu, F. Q.; Ai, X.; Zhang, X. T.; Cao, Y.; Yu, J. F.; Wu, T. H.; Bai, Y. B.; Li, T. J.; Tang, X. Y. *Appl. Catal., A* **1998**, *174*, 25−32.
(39) Chou, S. S.; Huang, C. P. *Appl. Catal., A* **1999**, *185*, 237−245.
(40) Chou, S. S.; Huang, C. P. *Chemosphere* **1999**, *38*, 2719−2731.
(41) Lu, M. C. *Chemosphere* **2000**, *40*, 125−130.
(42) Huang, H. H.; Lu, M. C.; Chen, J. N. *Water Res.* **2001**, *35*, 2291−2299.
(43) Cuzzola, A.; Bernini, M.; Salvadori, P. *Appl. Catal., B* **2002**, *36*, 231−237.
(44) Gurol, M. D.; Lin, S. S. *J. Adv. Oxid. Technol.* **2002**, *5*, 147−154.
(45) Kwan, W. P.; Voelker, B. M. *Environ. Sci. Technol.* **2002**, *36*, 1467−1476.
(46) Latifoglu, A.; Kilic, A. *Fresenius Environ. Bull.* **2002**, *11*, 894−898.
(47) Larpent, C.; Patin, H. *J. Mol. Catal.* **1992**, *72*, 315−329.
(48) Perathoner, S.; Centi, G. *Top. Catal.* **2005**, *33*, 207−224.
(49) Tyre, B. W.; Watts, R. J.; Miller, G. C. *J. Environ. Qual.* **1991**, *20*, 832−838.
(50) Watts, R. J.; Udell, M. D.; Monsen, R. M. *Water Environ. Res.* **1993**, *65*, 839−844.
(51) Kong, S. H.; Watts, R. J.; Choi, J. H. *Chemosphere* **1998**, *37*, 1473−1482.
(52) Valentine, R. L.; Wang, H. *J. Environ. Eng. (Reston, Va.)* **1998**, *124*, 31−38.
(53) Watts, R. J.; Teel, A. L. *J. Environ. Eng. (Reston, Va.)* **2005**, *131*, 612−622.
(54) Moura, F.; Oliveira, G. C.; Araujo, M. H.; Ardisson, J. D.; Macedo, W.; Lago, R. M. *Appl. Catal., A* **2006**, *307*, 195−204.

Table 1. Labeling and Specific Surface Areas of the Synthesized Iron(III) Oxide Catalysts

sample	calcination time (h)	specific surface area ($m^2 g^{-1}$), ±3%	sample	calcination time (h)	specific surface area ($m^2 g^{-1}$), ±3%
A	6	401	F	30	245
B	8	386	G	48	235
C	10	340	H	64	186
D	12	337	I	100	154
E	17	288			

minimum conversion temperature of 175 °C for various time periods (6−100 h), producing a range of nanoparticle surface areas. Labeling of the samples and their surface areas are listed in Table 1.

2.2. Catalyst Characterization. High-resolution transmission electron microscopy (HRTEM) was carried out on a JEOL JEM 3010 microscope operated at 300 kV (LaB6 cathode, point resolution 1.7 Å) equipped with an EDX (energy dispersive X-ray) detector. Images were recorded by a CCD camera at a resolution of 1024 × 1024 pixels using the Digital Micrograph software package. Powder samples were dispersed in ethanol, and the suspension was treated in a sonicator bath for 10 min. A drop of dilute suspension was placed on a holey-carbon-coated copper grid and allowed to dry at ambient temperature. The transmission ^{57}Fe Mössbauer spectra of 512 channels were collected using a Mössbauer spectrometer at constant acceleration mode with a ^{57}Co(Rh) source. The basic measurements were carried out at room temperature. In-field Mössbauer spectra used for distinguishing between amorphous and crystalline structures were recorded at 50 K in an external magnetic field of 5 T, applied parallel to the propagation of γ-rays, using a cryomagnetic Oxford Instruments system. The isomer shift values were referred to α-Fe at room temperature. An X'Pert PRO instrument with Co Kα radiation was employed for XRD analyses. The phase composition of the samples was evaluated using the X'Pert HighScorePlus software package (PANanalytical) and the JCPDS PDF-4 database. Surface areas were determined by nitrogen adsorption at 77.4 K by the static volumetric technique on a Sorptomatic 1990 (Thermo Finnigan) instrument. Prior to the measurements, the samples were degassed at 25 °C for at least 20 h, although outgassing pressures lower than 0.1 Pa were commonly reached after 2−4 h. The adsorption−desorption isotherms were measured up to the saturation pressure of nitrogen. The values of the specific surface area were determined by the multipoint BET3 method within the range 0.0−0.5 of relative pressures. The analysis was performed with the ADP 4.0 (CE Instruments) software package. Elemental analysis (C, H, O) checking the purity of the synthesized catalysts was performed with an EA Flash 1112 (Thermo Finnigan) elemental analyzer.

2.3. Kinetic Measurements of Catalytic Decomposition of Hydrogen Peroxide. A flask containing a mixture of hydrogen peroxide (c_0 = 0.02 M) and the studied catalyst (1 g L^{-1}) was shaken during reaction to provide sufficient dispersion of the catalyst particles. The pH of the reaction mixture was not adjusted by buffer solution to avoid reaction of •OH radicals with the buffer solution. The pH varied from 6.3 to 6.5 as expected for the reaction in distilled water under standard atmospheric conditions. Samples of solution taken at various time points were filtrated, and the hydrogen peroxide concentration was measured by the permanganate titration method. The decomposition of hydrogen peroxide in the presence of iron oxide-based catalysts follows a first-order rate law kinetics—$d[H_2O_2]/dt = k_{obsd}[H_2O_2]$ and thus $\ln([H_2O_2]/[H_2O_2]_0) = -k_{obsd}t$, where k_{obsd} is the observed first-order rate constant and $[H_2O_2]$ and $[H_2O_2]_0$ are the concentrations of hydrogen peroxide in the solution at any time t and at time zero, respectively.[44] This model was used for fitting the collected kinetic data. As predicted, the kinetics of catalyst-induced hydrogen peroxide decomposition obeyed first-order rate law kinetics documented by statistical analyses of kinetic curves (R^2 ranged from 0.99897 to 0.99988).

3. Effect of the Calcination Time on the Phase Composition, Crystallinity, and Particle Size of As-Prepared Nanoscopic Iron(III) Oxides. Mössbauer Spectroscopy, XRD, and HRTEM Analyses

The changes in the phase composition, crystallinity, and size of the iron(III) oxide nanoparticles prepared by various calcination times are clearly reflected in the room temperature (RT) Mössbauer spectra, where the spectral area of the magnetically split (sextet) component gradually increases at the expense of the superparamagnetic doublet. The RT Mössbauer spectra of the representative samples are shown in Figure 1; their hyperfine parameters are summarized in Table S (Supporting Information). Generally, no traces of divalent iron indicating any possible presence of undecomposed ferrous oxalate and/or an admixture of magnetite were observed in any of the spectra.

Samples prepared by shorter heating times, up to 12 h (A−D), are characterized by a rather broad doublet spectrum of a non-Lorentzian shape, reflecting a quadrupole splitting distribution. Such a non-Lorentzian doublet possessing very similar hyperfine parameters was previously observed in the Mössbauer spectra of amorphous Fe_2O_3 nanoparticles prepared by various routes.[55−58] Actually, the nanoparticles in sample A reveal almost completely amorphous character, a globular shape, and a size of 2−3 nm as confirmed by XRD (Figure 2, sample A) and HRTEM (Figure 3, sample A) analyses. With increasing calcination time between 6 and 17 h, diffraction peaks corresponding to hematite (α-Fe_2O_3) appear in XRD patterns; however, they are still very broad due to the very low dimension of the primarily formed hematite nanograins. These hematite nanoparticles are highly crystalline (see representative selected area electron diffraction, SAED, in Figure 3, sample D) and do not change considerably in their size (5−7 nm) during heating between 8 and 12 h (samples B−D). Thus, the complementary XRD and HRTEM data allow us to assume that the gradually increasing proportion of the crystalline phase at the expense of the amorphous phase is responsible for the decreasing surface area within samples A−D (see Table 1) rather than the gradual growth of the crystalline particles. This conclusion is also supported by the preservation of the general superparamagnetic character (Mössbauer doublet) of samples B−D, signaling that there is no drastic growth of the particle volume, which should be accompanied by the presence of a sextet component.

The RT Mössbauer spectra of the samples heated for longer periods of time (17−100 h, E−I) reveal, besides the previously discussed central superparamagnetic component, a magnetically split pattern fitted by two sextets, which can be ascribed to the hematite particles formed by the gradual growth (recrystallization) of the primarily formed α-Fe_2O_3 nanograins (see Figure 1). The presence of two sextets can be clearly ascribed to the extremely small hematite particles yielding different hyperfine parameters for the surface and bulk Fe(III) ions. Such diverse magnetic behavior of the surface and bulk iron atoms has been

(55) Machala, L.; Zboril, R.; Gedanken, A. *J. Phys. Chem. B* **2007**, *111*, 4003−4018.
(56) Ennas, G.; Musinu, A.; Piccaluga, G.; Zedda, D.; Gatteschi, D.; Sangregorio, C.; Stanger, J. L.; Concas, G.; Spano, G. *Chem. Mater.* **1998**, *10*, 495−502.
(57) Prozorov, T.; Prozorov, R.; Koltypin, Y.; Felner, I.; Gedanken, A. *J. Phys. Chem. B* **1998**, *102*, 10165−10168.
(58) Xu, X. N.; Wolfus, Y.; Shaulov, A.; Yeshurun, Y.; Felner, I.; Nowik, I.; Koltypin, Y.; Gedanken, A. *J. Appl. Phys.* **2002**, *91*, 4611−4616.

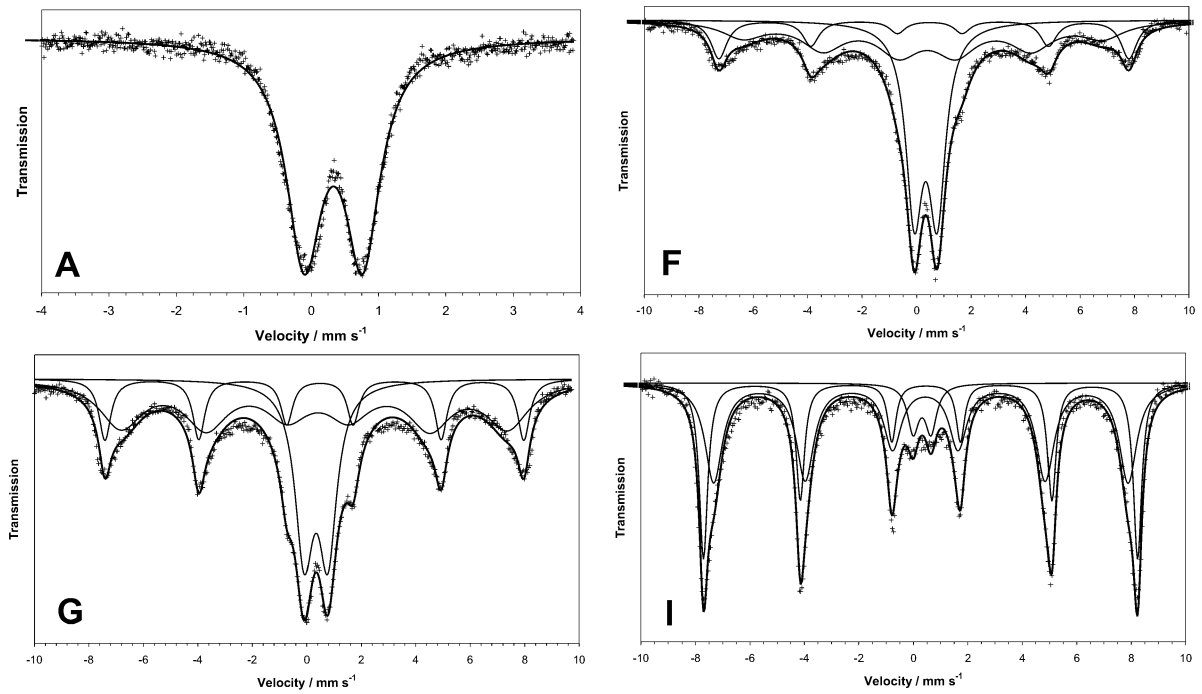

Figure 1. RT Mössbauer spectra of samples A, F, G, and I prepared by isothermal decomposition of $FeC_2O_4 \cdot 2H_2O$ at 175 °C for 6, 30, 48, and 100 h, respectively.

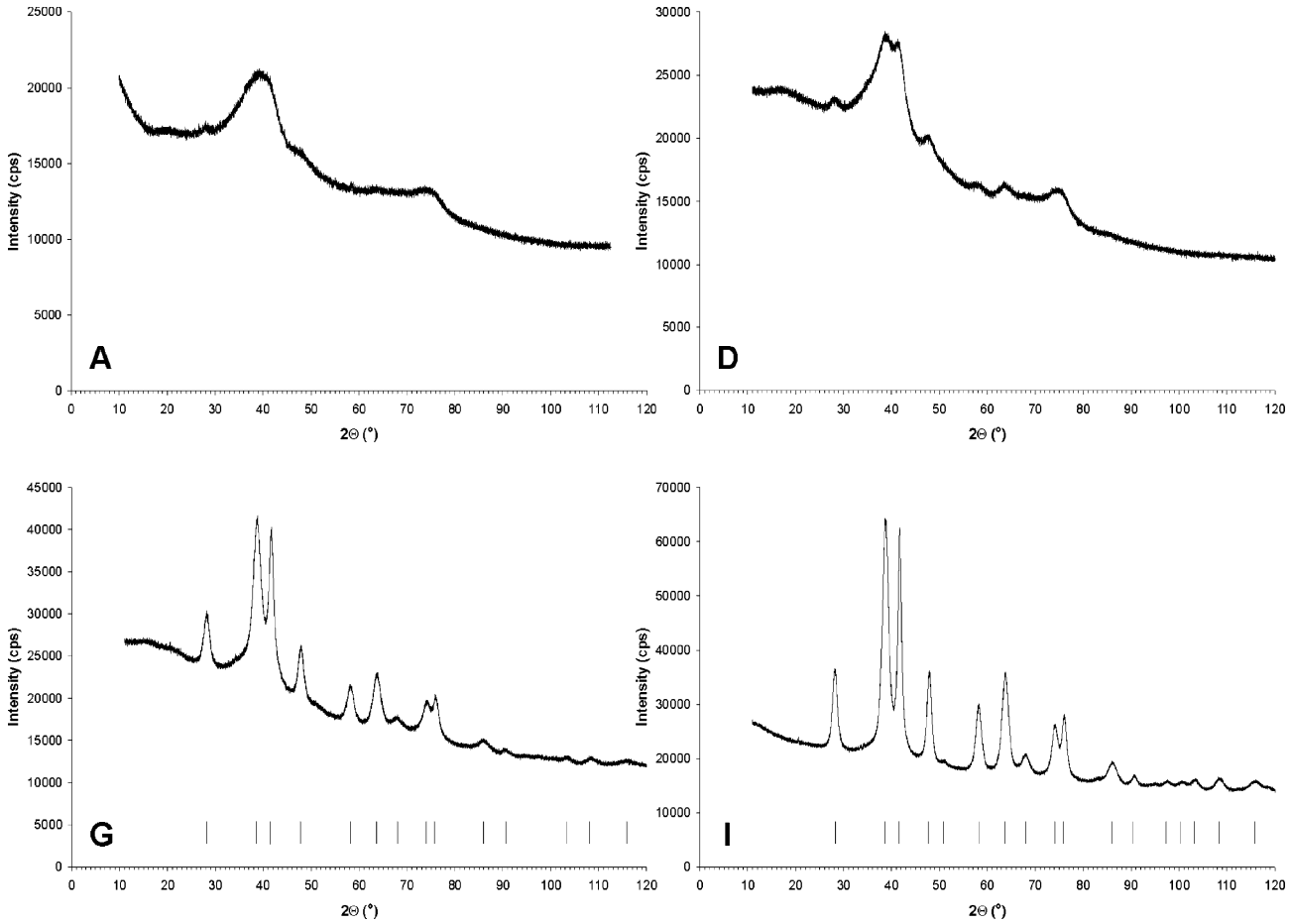

Figure 2. XRD patterns of representative samples A, D, G, and I demonstrating gradual crystallization of amorphous Fe_2O_3 to hematite and its consequent recrystallization with increasing calcination time.

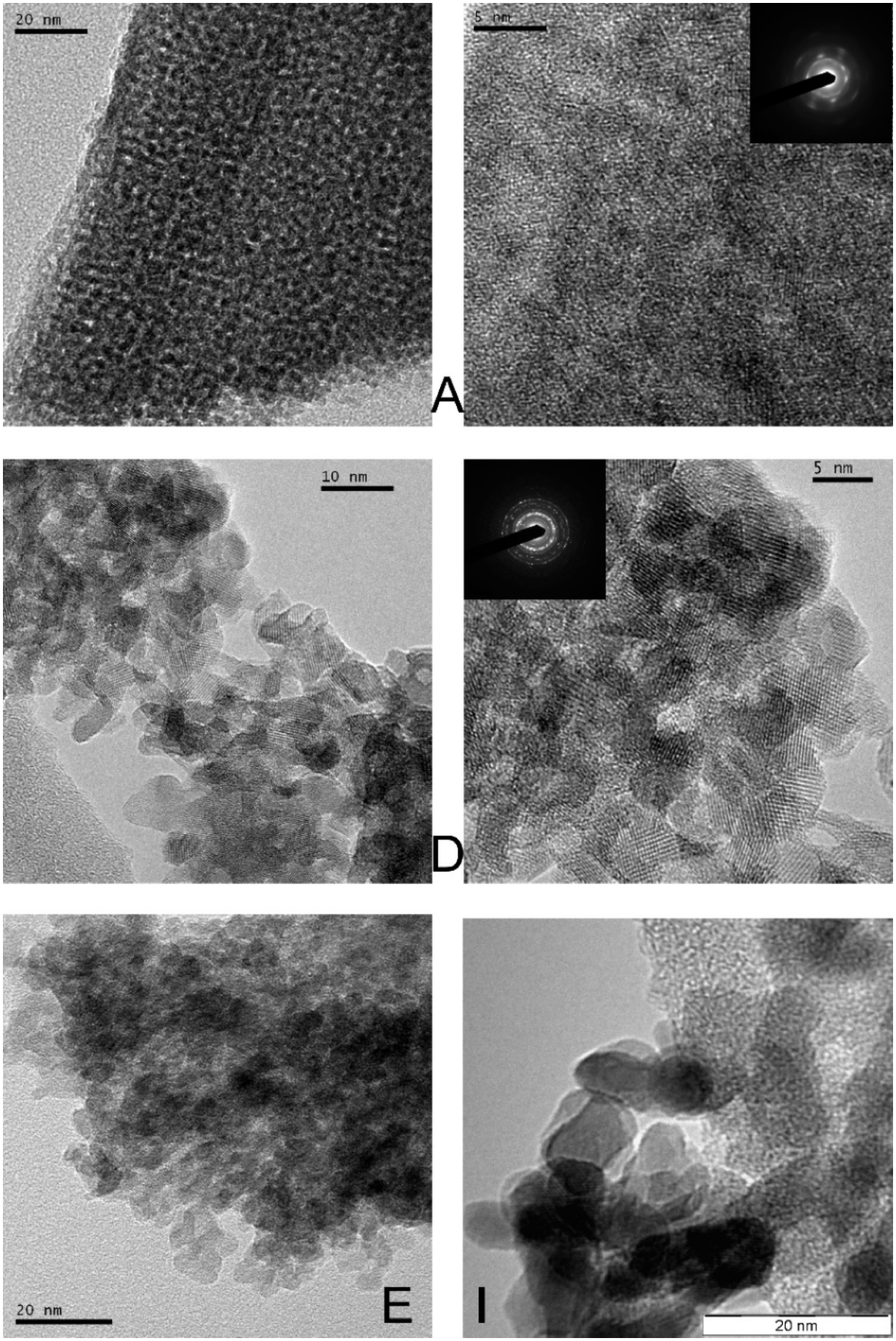

Figure 3. HRTEM and representative SAED images of samples A, D, E, and I.

reported for nanocrystalline hematite particles.[59] The sextet with the higher value of hyperfine magnetic field, having the isomer shift ($\delta = 0.37$ mm s^{-1}) and quadrupole shift ($\epsilon_Q = -0.21$ mm s^{-1}) parameters close to those reported for highly crystalline hematite, should be ascribed to the "bulk Fe(III)" ions,[60] while the second significantly broadened sextet exhibiting substantially lower H and higher deviations from ideal δ and ϵ_Q values (0.31−0.36 and −0.16 to −0.17 mm s^{-1}, respectively) corresponds to the "surface Fe(III)" ions. Clearly, the values of the hyperfine magnetic fields of both sextets observed at room temperature increase with calcination time (see Table S). Within samples E−I, one can also readily visualize (see Figure 1 and Table S) that the relative content of the central superparamagnetic component gradually decreases with the heating time in favor of both surface and bulk hematite sextets having together a final 93.4% of the spectrum area in sample I. The increasing hyperfine magnetic fields of both sextets, simultaneous mutual approach, and narrowing of the corresponding spectral lines are clear Mossbauer evidence of hematite particle growth in samples isothermally treated for 17−100 h. Corresponding HRTEM data allow the quantification of this calcination-time-dependent particle growth. As mentioned above, the primarily formed hematite nanograins are globular in shape and about 5−7 nm in diameter (see Figure 3, samples D and E), while the particles undergoing 100 h thermal treatment show sizes within 10−15 nm (see Figure 3, sample I). These values correspond well to the mean crystallite diameters estimated from the narrowing of the XRD lines according to the Scherrer formula: 5.9 nm for sample D and 12.1 nm for sample I.

All of the data mentioned above prove an occurrence of two competitive processes during sample calcination: (i) crystallization of amorphous Fe_2O_3 to hematite nanograins and (ii) thermally induced sintering of these grains and growth of the particles. As shown above, the latter process can be easily evaluated from the HRTEM and XRD data, while the first can hardly to be quantified using these techniques. However, quantification of the relative contents of amorphous Fe_2O_3 and nanocrystalline α-Fe_2O_3 phases with respect to calcination time reveals key information allowing full comprehension of the unique catalytic behavior of the synthesized nanopowders, further discussed in the next section.

We measured the Mössbauer spectra of representative samples A, D, and E at 50 K in an external magnetic field of 5 T applied parallel to the γ-ray propagation (see Figure 4 and Table S—spectra labeled A_1, D_1, and E_1). The temperature of measurement (50 K) was chosen a little below the magnetic ordering temperature of interacting amorphous Fe_2O_3 nanoparticles,[61] where their average hyperfine magnetic field is drastically reduced. This allows distinguishing the amorphous phase from hematite, as the latter exhibits a significantly higher effective magnetic field. Moreover, the amorphous Fe_2O_3 phase is easily detectable in the in-field spectrum as its subspectrum does not reveal any change in the line intensities when compared to the zero-field spectrum. This is due to its speromagnetic behavior below the magnetic ordering temperature, where the spins of the amorphous phase freeze in fixed directions relative to each other, without exhibiting any preferred orientation. Thus, the application of an external field does not induce any long-range ordering due to the absence of the principal crystallographic axis in an amorphous particle.[55,62,63] Contrary to the amorphous phase, hematite exhibits noticeably enhanced intensities of the second and fifth spectral lines at the chosen measuring geometry because of its predominantly antiferromagnetic behavior.[64]

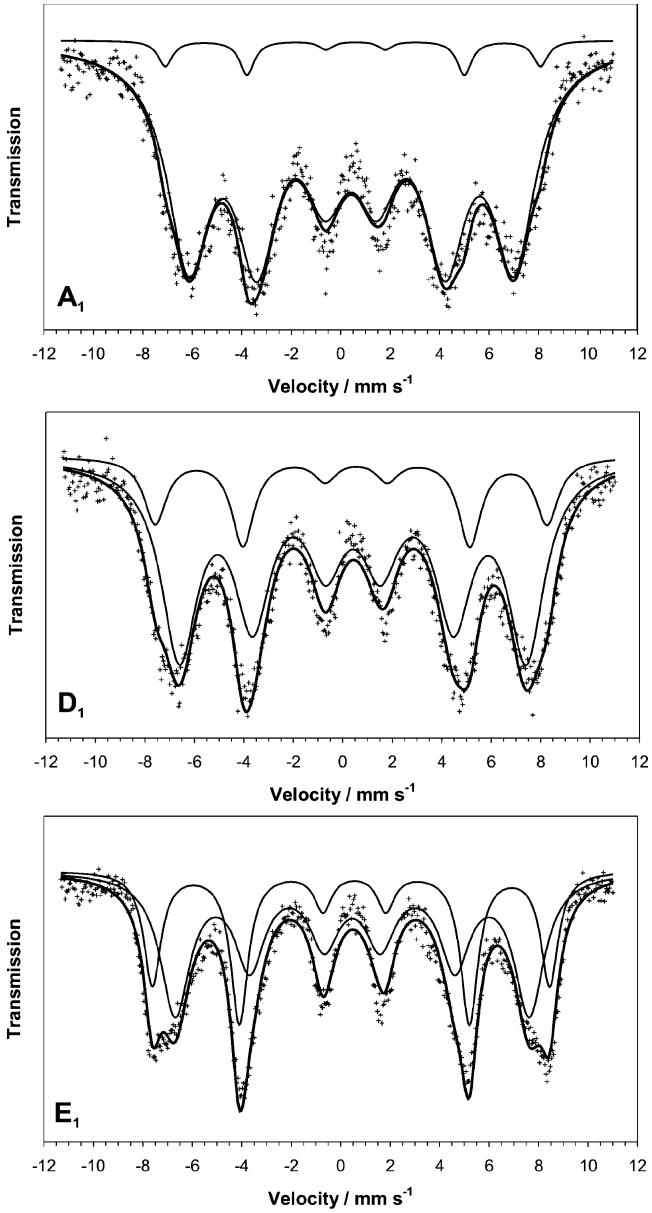

Figure 4. Mössbauer spectra of representative samples A, D, and E taken at 50 K in the external magnetic field of 5 T applied parallel to the γ-ray propagation.

With an assumption of these substantial differences in magnetic behavior of amorphous Fe_2O_3 and α-Fe_2O_3, we fitted the in-field Mössbauer spectra of samples A, D, and E as shown in Figure 4. Indeed, the spectra are well fitted by two sextets differing mainly in effective magnetic fields and line intensities. The first component with a significantly lower value of H_{eff} (41−44 T) can be clearly ascribed to amorphous Fe_2O_3. The

(59) Murad, E. *Phys. Chem. Miner.* **1996**, *23*, 248−262.
(60) Zboril, R.; Mashlan, M.; Petridis, D. *Chem. Mater.* **2002**, *14*, 969−982.
(61) Zboril, R.; Machala, L.; Mashlan, M.; Sharma, V. *Cryst. Growth Des.* **2004**, *4*, 1317−1325.
(62) Coey, J.; Readman, P. W. *Nature* **1973**, *246*, 476−478.
(63) Guerault, H.; Tamine, M.; Greneche, J. M. *J. Phys.: Condens. Matter* **2000**, *12*, 9497−9509.
(64) Pankhurst, Q. A.; Pollard, R. J. *J. Phys.: Condens. Matter* **1990**, *2*, 7329−7337.

significant broadening of this sextet reflects a distribution of effective magnetic fields related to various degrees of distortion of oxygen octahedra having the respective symmetry axis randomly orientated in a nonperiodic lattice.[61] The nearly zero value of the quadrupole shift indicates a random distribution of angles between the magnetic hyperfine field and the electric field gradient. The second magnetically split component with noticeably enhanced intensities of the second and fifth spectral lines is much narrower and possesses a higher effective magnetic field (47−49 T), as expected for hematite. A negative quadrupole shift ranging from −0.11 to −0.20 mm/s confirms its weakly ferromagnetic nature above the Morin transition temperature. Such drastic reduction of the Morin transition temperature (normally 260 K) is often observed in systems of hematite nanoparticles with a size below 20 nm.[60] As the most important conclusion, the spectral area of the hematite sextet increases from ca. 5% in sample A to 22% in sample D and to 37% in sample E. This unambiguously confirms the gradually increasing crystallinity between samples A and E, which is, in our opinion, responsible for the unique escalation of the catalytic efficiency of the samples (see the next section).

4. Catalytic Efficiency of Iron(III) Oxide Nanopowders

The present literature data show that the surface area is the principal parameter affecting the catalytic efficiency of iron oxides in decomposition of hydrogen peroxide. Specific surface areas of samples A−I were measured by the conventional BET method where all obtained isotherms are qualitatively of the same type, IIb (according to the IUPAC classification); the shape is generally associated with monolayer−multilayer adsorption on an open and stable external surface of a powder consisting of nonporous particles.[65]

The hysteresis observed in all measured samples is of a type, H_3 (IUPAC), that is commonly associated with the platelike aggregates of particles possessing nonrigid slits. In such a case the desorption curve follows a path different from that of the adsorption isotherm branch from high p/p^0 (delayed capillary condensation) until a critical p/p^0 is reached (unstable condensate).[65]

This behavior is entirely consistent with the morphological character of the prepared iron(III) oxide nanopowders consisting of dense platelike agglomerates of ultrasmall particles (see the TEM image in Figure 3, sample A). In this sense and with respect to the isotherm type (IIb, nonporous sample), we interpret the observed hysteresis loops as a consequence of interparticle spaces in the aggregates of iron oxide nanoparticles.

Representative isotherms of samples A and D are presented in Figure 5.

Numerical values calculated using the BET3 method (full or three-parameter equation) within an interval of the relative pressures p/p^0 of 0−0.5 are summarized in Table 1. The obtained data show the gradual decrease of the surface area with calcination time as one would naturally expect due to the growth of the particles caused by thermally induced crystallization.

Truly astonishing, however, are the obtained values of the rate constants, in particular their dependence on the surface area (Figure 6a) and on the calcination time (Figure 6b). Following the assumption of the dominant role of the surface area, the highest catalytic efficiency should be achieved with the sample

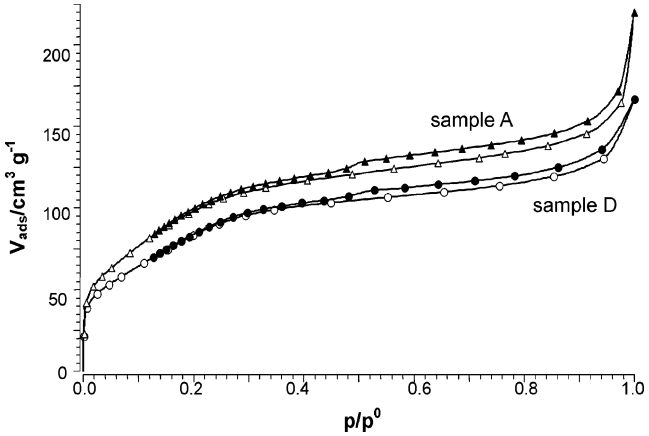

Figure 5. Adsorption−desorption isotherms of samples A and D.

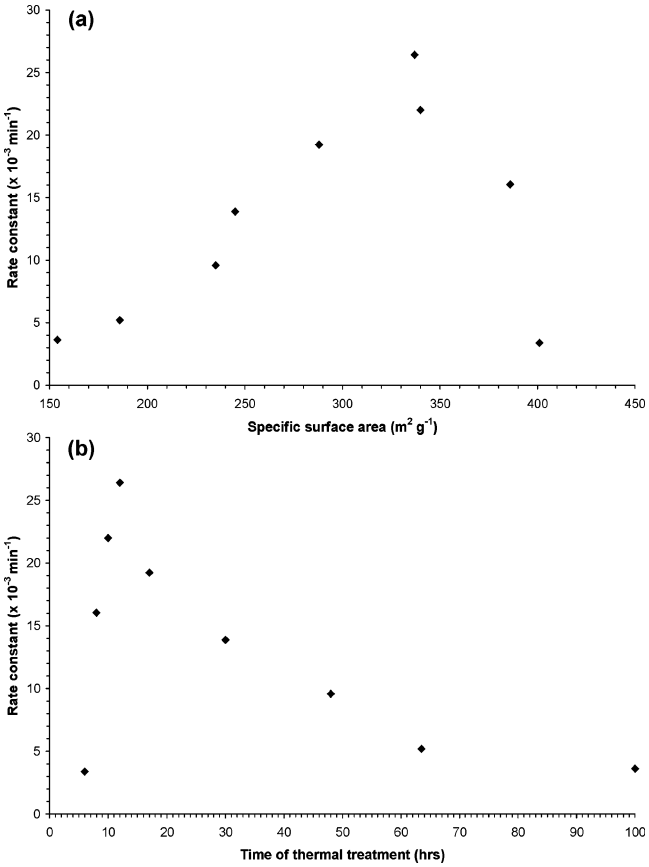

Figure 6. Dependence of the rate constants on the specific surface area (a) and calcination time (b) for the synthesized Fe_2O_3 catalysts.

exhibiting the largest value equal to 401 $m^2\ g^{-1}$ (sample A), which moreover represents one of the largest surface areas so far published for Fe_2O_3-based catalysts. Surprisingly, the recorded rate constant of this sample is the lowest among all measured (Figure 6a). The unusual catalytic behavior is also manifested by the huge increase of the rate constant in samples A−D, which is accompanied by the simultaneous decrease in surface area. For sample D (surface area of 337 $m^2\ g^{-1}$), the rate constant normalized with the catalyst concentration reaches its maximum of 26.41 × 10^{-3} $min^{-1}(g/L)^{-1}$, which is the highest catalytic efficiency so far achieved for decomposition of hydrogen peroxide on iron oxides, independent of the pH conditions.

(65) Ananieva, E.; Reitzmann, A. *Chem. Eng. Sci.* **2004**, *59*, 5509−5517.

Toward longer calcination times (samples E−I), the rate constant behaves as commonly known in heterogeneous catalysis based on iron oxides—gradually decreasing with decreasing surface area. This is an expected result of the thermal recrystallization of primarily formed hematite nanoparticles accompanied by a gradual increase in the particle size (see the HRTEM images in Figure 3).

It is worth mentioning that all tested iron(III) oxide catalysts did not contain any traces of the oxalate precursor as proved by XRD, Mössbauer spectroscopy, and elemental analysis (C and H contents). Moreover, the adsorption−desorption isotherms of samples A−D exhibit the same qualitative character (see Figure 5), confirming the same nonporous nature of the analyzed nanopowders. These facts unambiguously exclude the possible responsibility of the precursor admixture and/or the sample porosity for the unusual increase in the catalytic activity with decreasing surface area.

Thus, the observed unconventional nonmonotone dependence of the rate constant on the surface area (Figure 6a) reveals a unique phenomenon, which has not been reported so far in either decomposition of hydrogen peroxide or other reaction systems catalyzed by iron oxide nanoparticles. On the grounds of the previously discussed in-field Mössbauer, XRD, and HRTEM data, this behavior can be ascribed to the key role of increasing crystallinity prevailing over the catalytic effect of the surface area as shown in samples A−D.

According to our best knowledge, the mentioned local increase in the catalytic efficiency with increasing catalyst crystallinity has recently been reported in two processes of heterogeneous catalysis. Thus, the catalytic efficiency of a nanoamorphous Ni−B alloy consecutively annealed at various temperatures and tested in benzene hydrogenation proved to be dependent on the annealing temperature; the benzene conversion continually increased with increasing calcination temperature of the catalyst and reached its maximum of 63% for a catalyst annealed at 623 K, which was more than twice as much compared to that of the originally prepared nanoamorphous alloy. A further increase in the annealing temperature of the catalysts resulted in a decrease of the benzene conversion degree.[66] The influence of catalyst crystallinity was also observed in conversion of propane performed with Zn/Ga/H-ZSM-5-based catalysts[67]or with Mo−V−Te−Nb mixed oxides prepared at various pH values.[68] In both cases increasing catalytic activity was achieved with increasing degree of crystallinity of the as-prepared catalysts.

It seems therefore that besides the commonly accepted catalytic effect of the surface area there is a more complex factor of the "surface quality" of the catalysts that substantially drives the catalytic efficiency. Apart from the principal role of the sample crystallinity confirmed in this study, other qualitative parameters can include the chemical composition of the catalyst[42] and the particle morphology. The effect of the particle shape was described in the recent study on quasicubic hematite nanoparticles exhibiting a significantly higher catalytic performance in catalytic oxidation of carbon monoxide than those nanophases with flowerlike, hollow, or other irregular external morphologies.[69] This is an indirect support of our conclusions that the exposure of the crystal planes of the catalysts can affect the processes of heterogeneous catalysis more significantly than traditionally accepted factors such as a high BET surface area. A study evaluating the effect of the crystal structure of iron(III) oxide catalysts (α-, β-, γ-, and ϵ-Fe_2O_3), after normalization with the surface area, is in progress.

Acknowledgment. This work was supported by the Projects of the Ministry of Education of the Czech Republic (1M619895201 and MSM6198959218). We thank Mariana Klementova from the Electron Microscopy Group of the Institute of Inorganic Chemistry at the Academy of Sciences of the Czech Republic in Rez near Prague for the HRTEM measurements and Yekaterina Krasnova from the Florida Institute of Technology, Faculty of Chemistry, Florida, for proofreading the manuscript.

Supporting Information Available: Table S, Mössbauer parameters of iron(III) oxide samples prepared by thermal decomposition of $FeC_2O_4 \cdot 2H_2O$ at 175 °C for different periods of time. This material is available free of charge via the Internet at http://pubs.acs.org.

JA072918X

(66) Jiang, Z.; Yang, H. W.; Wei, Z.; Xie, Z.; Zhong, W. J.; Wei, S. Q. *Appl. Catal., A* **2005**, *279*, 165−171.
(67) Nicolaides, C. P.; Sincadu, N. P.; Scurrell, M. S. *Catal. Today* **2002**, *71*, 429−435.
(68) Oliver, J. M.; Nieto, J.; Botella, P.; Mifsud, A. *Appl. Catal., A* **2004**, *257*, 67−76.
(69) Zheng, Y. H.; Cheng, Y.; Wang, Y. S.; Bao, F.; Zhou, L. H.; Wei, X. F.; Zhang, Y. Y.; Zheng, Q. *J. Phys. Chem. B* **2006**, *110*, 3093−3097.